Geophysical Research Letters

RESEARCH LETTER
10.1029/2023GL105470

Key Points:

- Atmospheric gravity waves can generate plasma ducts and irregularities in the plasmasphere using the coupled SAMI3/WACCM-X model
- The electron density in the equatorial plasmasphere is irregular as a function of longitude
- Plasma ducts can be generated for L-shells in the range 1.5–3.0 with lifetimes of 0.5–2.0 hr

Correspondence to:

J. D. Huba,
jdhuba@syntek.org

Citation:

Huba, J. D., & Liu, H.-L. (2023). Modeling the development of plasmasphere ducts and irregularities with SAMI3/WACCM-X. *Geophysical Research Letters*, *50*, e2023GL105470. https://doi.org/10.1029/2023GL105470

Received 25 JUL 2023
Accepted 22 SEP 2023

Modeling the Development of Plasmasphere Ducts and Irregularities With SAMI3/WACCM-X

J. D. Huba[1] and **H.-L. Liu**[2]

[1]Syntek Technologies, Fairfax, VA, USA, [2]High Altitude Observatory, NCAR, Boulder, CO, USA

Abstract We show that atmospheric gravity waves can generate plasma ducts and irregularities in the plasmasphere using the coupled SAMI3/WACCM-X model. We find the equatorial electron density is irregular as a function of longitude which is consistent with CRRES measurements (Clilverd et al., 2007, https://doi.org/10.1029/2007ja012416). We also find that plasma ducts can be generated for L-shells in the range 1.5–3.0 with lifetimes of $\sim$ 0.5 hr; this is in line with observations of ducted VLF wave propagation with lifetimes of 0.5–2.0 hr (Clilverd et al., 2008, https://doi.org/10.1029/2007ja012602; Singh et al., 1998, https://doi.org/10.1016/s1364-6826(98)00001-7).

Plain Language Summary Electromagnetic plasma waves, known as whistler waves, are observed to propagate in the ionosphere/plasmasphere system where the ionosphere is nominally defined as the partially ionized gas surrounding the earth in the altitude range 90–1,000 km and the plasmasphere is essentially the extension of the ionosphere 1,000s of km into space along closed geomagnetic field lines. Whistler wave propagation has been characterized as ducted and non-ducted. Ducted propagation is guided along the magnetic field by density tubes in which the plasma density is lower or higher than the background plasma. However, the physical processes that generate these ducts has remained unclear. We show that these plasma ducts can be generated by atmospheric gravity waves that perturb the ionosphere and plasmasphere electron density using the coupled SAMI3/WACCM-X model.

1. Introduction

The plasmasphere is essentially the extension of the ionosphere into the inner magnetosphere along closed field lines. It is a relatively dense ($n_e > 10^2$ cm^{-3}), cold plasma ($T \lesssim 4 \times 10^4$ K) (Lemaire et al., 1998). The boundary between the plasmasphere and inner magnetosphere is the plasmapause and is typically defined as a steep drop in the plasma density (Carpenter, 1963, 1966; Goldstein et al., 2003). The conventional perception of the plasmasphere based on modeling studies is that it has a smooth toroidal shape (i.e., donut-like) under quiet geomagnetic conditions (e.g., see Figure 2 of Huba and Krall (2013)). On the other hand, during geomagnetic storms the plasmasphere undergoes "erosion" (the plasmapause moves closer to the earth) and develops a "plume-like" structure in the afternoon/dusk sector as well as "notches." (Goldstein, 2006; Sandel et al., 2001, 2003).

However, numerous studies of whistler wave propagation in the low- to mid-latitude ionosphere/plasmasphere system contrast "ducted" versus "non-ducted" wave propagation where ducts are nominally 10%–20% increases or decreases in the electron density along the geomagnetic field over relatively small length scales (10–100s km) (Bernhardt & Park, 1977; Clilverd et al., 2008; Lester & Smith, 1980; Singh et al., 1998; Sonwalkar, 2006; Strangeways, 1982). Additionally, there have been observations of plasmaspheric ducts from radio-interferometric measurements (Helmboldt, 2020a; Helmboldt et al., 2020; Jacobson et al., 1996; Loi et al., 2015) and density structures from satellite observations (Darrouzet et al., 2009) indicating that the inner plasmasphere is not spatially smooth as often characterized.

Several theories have been suggested for the cause of plasmasphere irregularities. Cole (1971) suggested spatially varying electric fields orthogonal to the magnetic field generating an interchange instability. Helmboldt et al. (2020) proposed variations in the neutral wind (caused by gravity waves) could generate electric field fluctuations that lead to density irregularities. They modeled this using a framework from SAMI2 (Huba et al., 2000) and with the background plasmaspheric electron density specified by the empirical model of Ozhogin et al. (2012) and an analytical model of gravity waves. They also suggested electro-buoyancy waves driven by an E region instability (Cosgrove & Tsunoda, 2002; Perkins, 1973; Yokoyama et al., 2009). In particular, Helmboldt (2020b) used GPS and SuperDARN data from Japan to demonstrate the connection of E region irregularities and corotating plasmaspheric irregularities. We note that the aforementioned instability mechanisms only apply to nighttime conditions and cannot explain the formation of ducts in the daytime.

We show that atmospheric gravity waves can generate plasma ducts and irregularities in the plasmasphere using the coupled SAMI3/WACCM-X model. Physically, gravity waves perturb the zonal and meridional neutral winds which affect the plasma motion and electric field. Since the magnetic field lines are equipotentials, the perturbed electric field maps into the plasmasphere and can generate duct and irregularities. We find the equatorial electron density is irregular as a function of longitude which is consistent with CRRES measurements (Clilverd et al., 2007). We also find that plasma ducts can be generated for *L*-shells in the range 1.5–3.0 with lifetimes of 0.5 hr; this is consistent with observations of ducted VLF wave propagation with lifetimes of 0.5–2.0 hr (Clilverd et al., 2008; Singh et al., 1998).

2. Models and Theory

WACCM-X is an atmospheric component of the National Center for Atmospheric Research (NCAR) Community Earth System Model, which couples atmosphere, ocean, land surface, sea and land ice, and carbon cycle components through exchanging fluxes and state information (Hurrell et al., 2013). It is based on the Community Atmosphere Model and WACCM. The first version of WACCM-X is described by H.L. Liu et al. (2010) and the most recent version is described in H.L. Liu et al. (2018). SAMI3 (Sami3 is Also a Model of the Ionosphere) is a seamless, global, three-dimensional, physics-based model of the ionosphere/plasmasphere system based on SAMI2 (Huba et al., 2000). Details of SAMI3 are described in Huba and Joyce (2010). The codes are one-way coupled in that WACCM-X provides the neutral composition, temperature, and winds as inputs to SAMI3 but SAMI3 does not provide ion densities or velocities to WACCM-X.

The simulation parameters are the same as used in Huba and Liu (2020) for the "March case." We consider the day March 21 for low solar activity conditions (F10.7 = 70 and F10.7A). The WACCM-X grid is 0.474° × 0.625° in latitude and longitude, and covers the entire earth. The SAMI3 grid is also 0.625° in longitude but is variable in latitude. The grid in latitude is ~1° for mid-latitudes (~40°), decreases to ~0.15° near the magnetic equator, and increases to ~1.5° in the high-latitude region. The SAMI3 grid in latitude is ±80° in magnetic coordinates. The high-latitude convection potential is specified by the Weimer05 model (Weimer, 2005).

We performed two sets of simulations. The first uses the coupled SAMI3/WACCM-X model as described above. The second uses the empirical thermosphere models NRLMSISE0 (Picone et al., 2002) for the neutral composition and temperature, and HWM14 (Drob et al., 2008) for the winds. The key reason for this is that WACCM-X includes atmospheric gravity waves while the empirical models do not; we can therefore compare the results of these two simulations to assess the role of atmospheric waves on the behavior of the plasmasphere. As shown in Huba and Liu (2020), atmospheric waves played an important role in the generation of equatorial plasma bubbles; they did not develop using the empirical thermosphere models.

As described in Huba et al. (2015), the primary influence of gravity-wave induced neutral wind variations on the ionosphere is determined by the velocity equation

$$\frac{\partial \mathbf{V}_i}{\partial t} + \mathbf{V}_i \cdot \nabla \mathbf{V}_i = -\frac{1}{\rho_i}\nabla \mathbf{P}_i + \frac{e}{m_i}\mathbf{E}$$

$$+\frac{e}{m_i c}\mathbf{V}_i \times \mathbf{B} + \mathbf{g} - \nu_{in}(\mathbf{V}_i - \mathbf{V}_\mathbf{n}) - \sum_j \nu_{ij}(\mathbf{V}_i - \mathbf{V}_j) \tag{1}$$

and the potential equation

$$\nabla \cdot (\Sigma \cdot \nabla \Phi) = S(V_n, g). \tag{2}$$

where the electric field is $\mathbf{E} = -\nabla\Phi$. In the above, the variables have their usual meaning and Equation 2 is fully defined in Huba and Joyce (2010). The variations in $\mathbf{V}_n$ affect the ion velocity along the magnetic field through the ion-neutral collision term $\nu_{in}\mathbf{V}_n$ in Equation 1. Clearly the importance of this term depends on $\mathbf{V}_n \cdot \mathbf{B}$ and is related to the direction of propagation of the gravity wave relative to the direction of the geomagnetic field. The variations in $\mathbf{V}_n$ transverse to $\mathbf{B}$ affect the ion velocity perpendicular to the magnetic field through the $\mathbf{E} \times \mathbf{B}$ drift associated with the dynamo-generated electric field from Equation 2, and this electric field maps along the

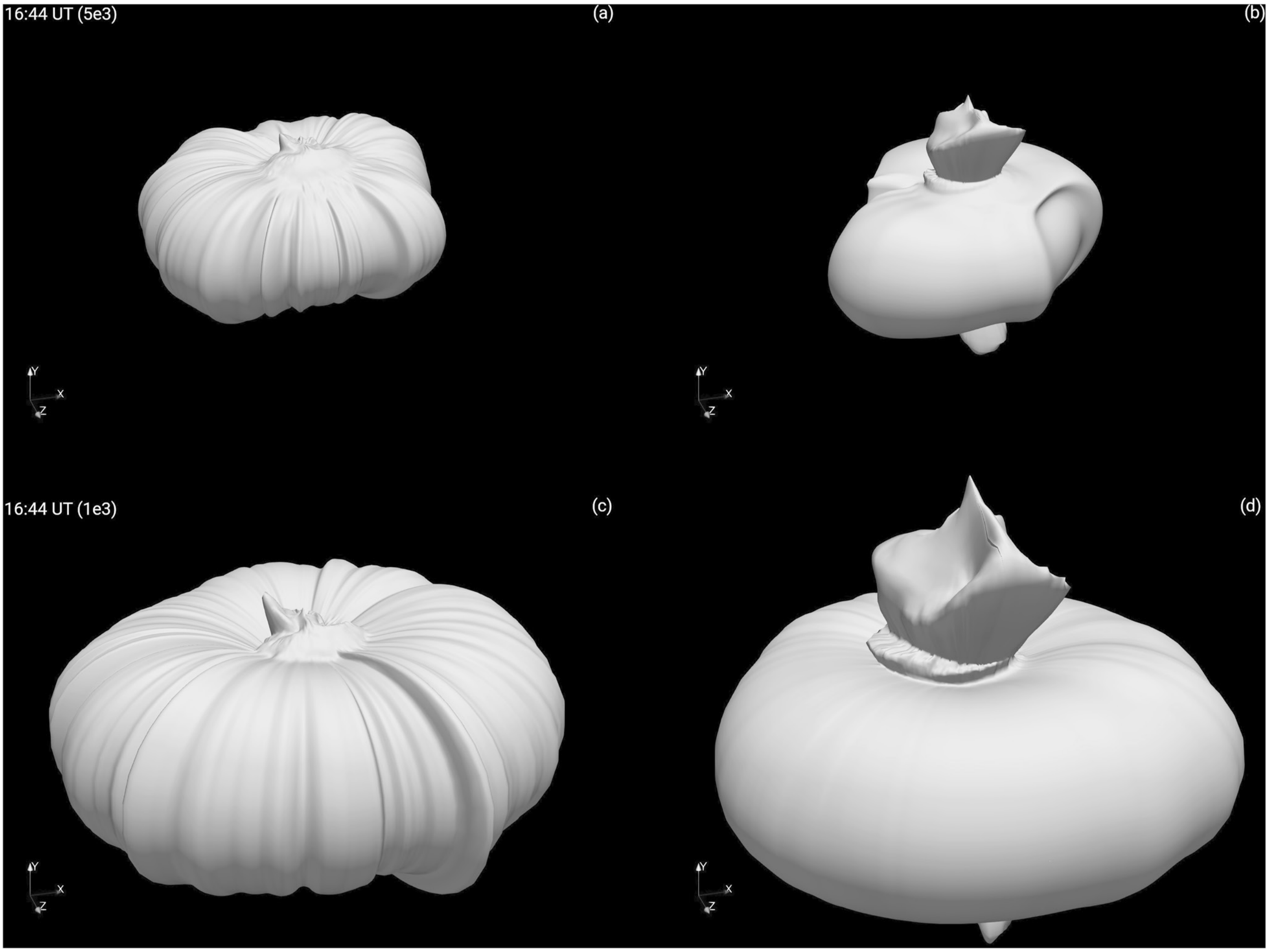

Figure 1. Isosurfaces of the electron density at $n_e = 5 \times 10^3$ cm^{-3} (a, b) and $n_e = 10^3$ cm^{-3} (c, d) at 16:44 UT. The isosurfaces in the top panels (a, b) are at $L \sim 2$ while the isosurfaces in the bottom panels (c, d) are at $L \sim 4$. The left panels (a, c) are for the SAMI3/WACCM-X simulation and the right panels (b, d) are for the SAMI3/NRLMSISE0/HWM14 simulation.

magnetic field to the conjugate region. Again, the importance of this effect is related to the direction of propagation of the gravity wave relative to the direction of the geomagnetic field.

3. Results

In Figure 1 we show isosurfaces of the electron density at $n_e = 5 \times 10^3$ cm^{-3} (a, b) and $n_e = 10^3$ cm^{-3} (c, d) at 16:44 UT. The isosurfaces in Figures 1a and 1b are at $L \sim 2$ while the isosurfaces in Figures 1c and 1d are at $L \sim 4$. The left panels (a, c) are for the SAMI3/WACCM-X simulation and the right panels (b, d) are for the SAMI3/NRLMSISE0/HWM14 simulation. In these panels the sun is in the $+z$-direction. The obvious difference between the two simulations is the corrugations in the electron density isosurface for the SAMI3/WACCM-X case which is attributed to atmospheric waves. In Figure 1b the electron density isosurface is smooth but there is a stronger longitudinal dependence associated with the diurnal behavior of the system. On the other hand, the over shape and extent of the plasmasphere is similar in Figures 1c and 1d except for the corrugated structure in Figure 1c. (As several colleagues have noted - the plasmasphere shape is more of a pumpkin than a donut.) Lastly, the outflow of plasma in the high latitude, polar cap region is different; this is attributed to differences in the neutral composition between the two cases.

In Figure 2 we plot the electron density as a function of longitude at 16:44 UT for (a) $L = 2$ and (b) $L = 4$. The black curves correspond to the SAMI3/WACCM-X case and the red curves correspond to the SAMI3/NRLMSISE0/HWM14 case. In Figure 2a there are small scale electron density irregularities in longitude

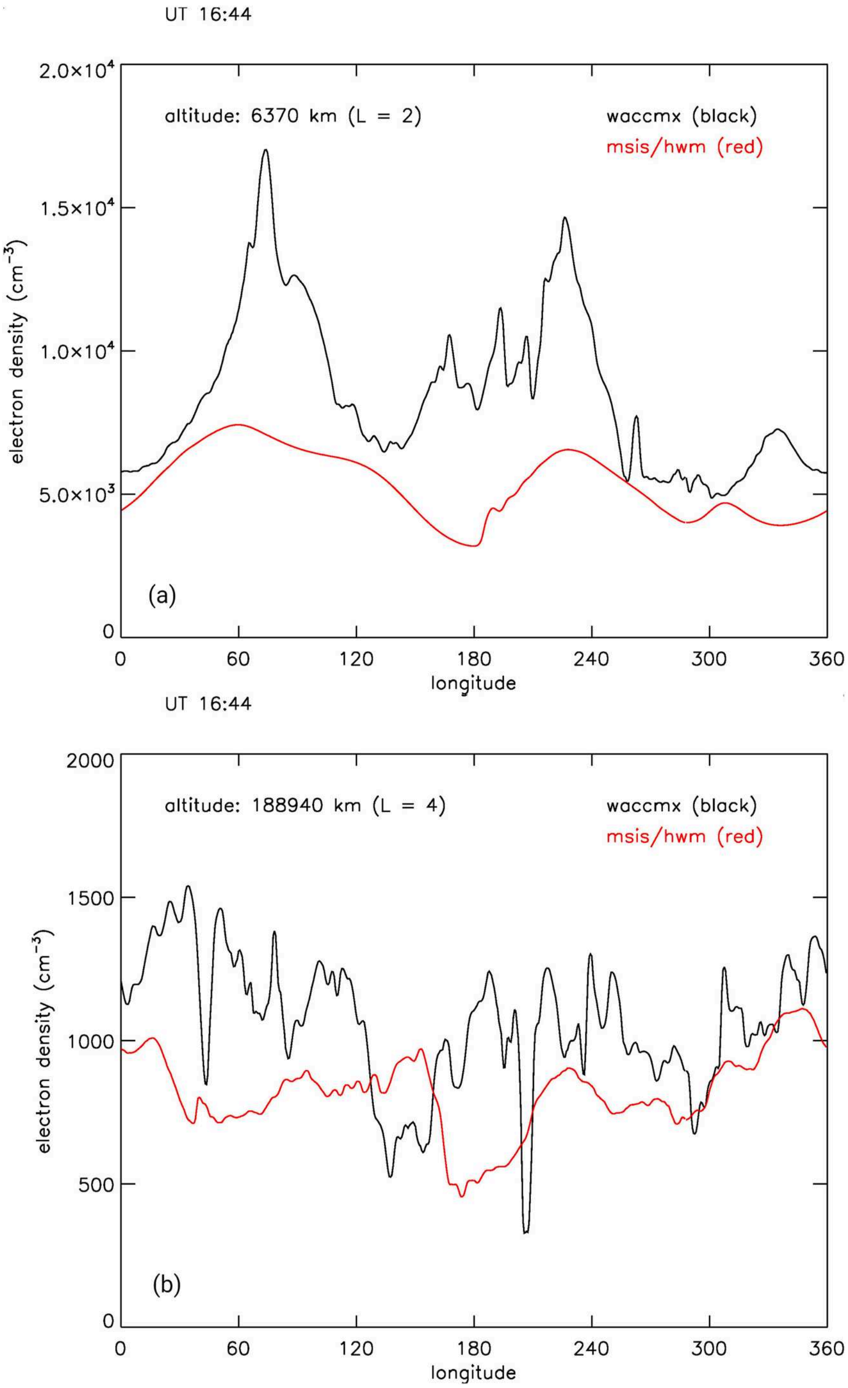

Figure 2. Line plots of the electron density as a function of longitude at 11:59 UT for (a) $L = 2$ and (b) $L = 4$. The black curves correspond to the SAMI3/WACCM-X case and the red curves correspond to the SAMI3/NRLMSIS/HWM14 case.

(a few degrees) for the WACCM-X case while the electron density is relatively smooth for the NRLMSISE0/HWM14 case. The large scale variation is associated with the diurnal behavior of the plasmasphere. On the other hand, in Figure 2b there is no obvious structure associated with diurnal behavior. In the WACCM-X case there are small (few degrees) and medium (~10°) scale electron density irregularities about an average density $n_e \sim 1{,}100$ cm^{-3}. In the NRLMSISE0/HWM14 case there are electron density fluctuations about an average density $n_e \sim 800$ cm^{-3} but they are much weaker than the WACCM-X case and are associated with variations in the high-latitude convection potential.

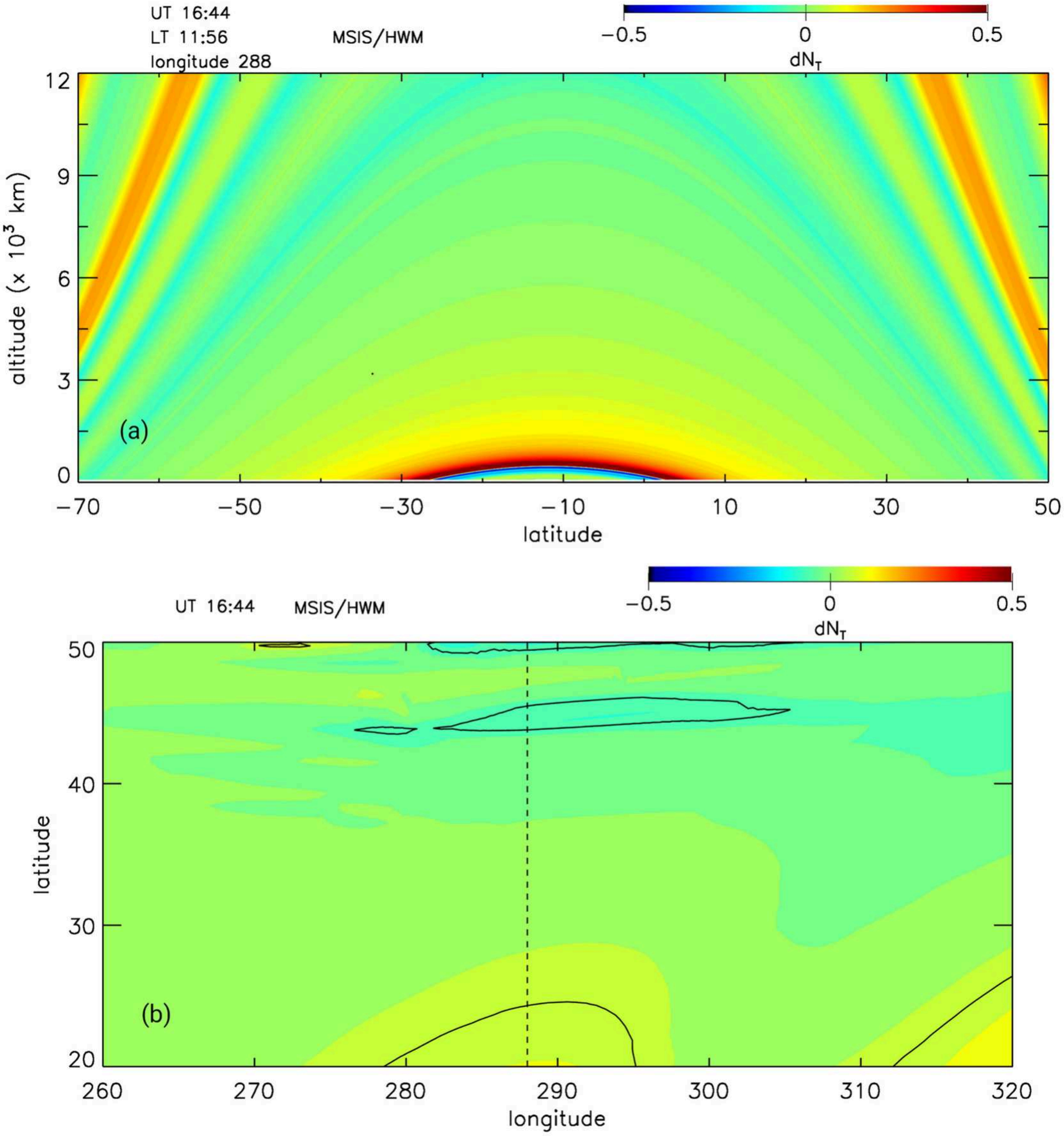

Figure 3. Contour plots of dN_T for MSIS/HWM at time 16:44 UT as a function of (a) latitude and altitude at longitude 288° (corresponds to 11:56 LT) and (b) longitude and latitude at the base of the field lines.

In assessing duct formation as it relates to whistler wave propagation we calculate the total electron content along a magnetic flux tube (Singh et al., 1998)

$$\mathrm{N_T} = \int_{1000S}^{1000N} n_e(s)\frac{B_0}{B_s}\, ds \tag{3}$$

where we integrate along a flux tube from an altitude of 1,000 km in the southern hemisphere (1000S) to an altitude of 1,000 km in the northern hemisphere (1000N), s is the coordinate along the flux tube, $n_e(s)$ is the electron density, $B_0 = 0.31$ G is the reference field, and B_s is the magnetic field along the flux tube. We also calculate $\mathrm{dN_T} = \mathrm{N_T} - \mathrm{N_{avgT}}$ where $\mathrm{N_{avgT}}$ is the $\mathrm{N_T}$ averaged over a 30 min window. This technique is similar to identifying traveling ionospheric disturbances in data and model results (e.g., Vadas et al., 2023).

In Figure 3 we show contour plots of $\mathrm{dN_T}$ for the NRLMSISE0/HWM14 case at time 16:44 UT as a function of (a) latitude and altitude at longitude 288° and (b) longitude and latitude at the base of the field lines in the ionosphere. In Figure 3a there are essentially no "ducts", localized regions of variations in $\mathrm{dN_T}$, at mid-latitudes (−70° to −30° and 10°–50°). The ducts at high-latitudes are associated with variations in the high-latitude convection

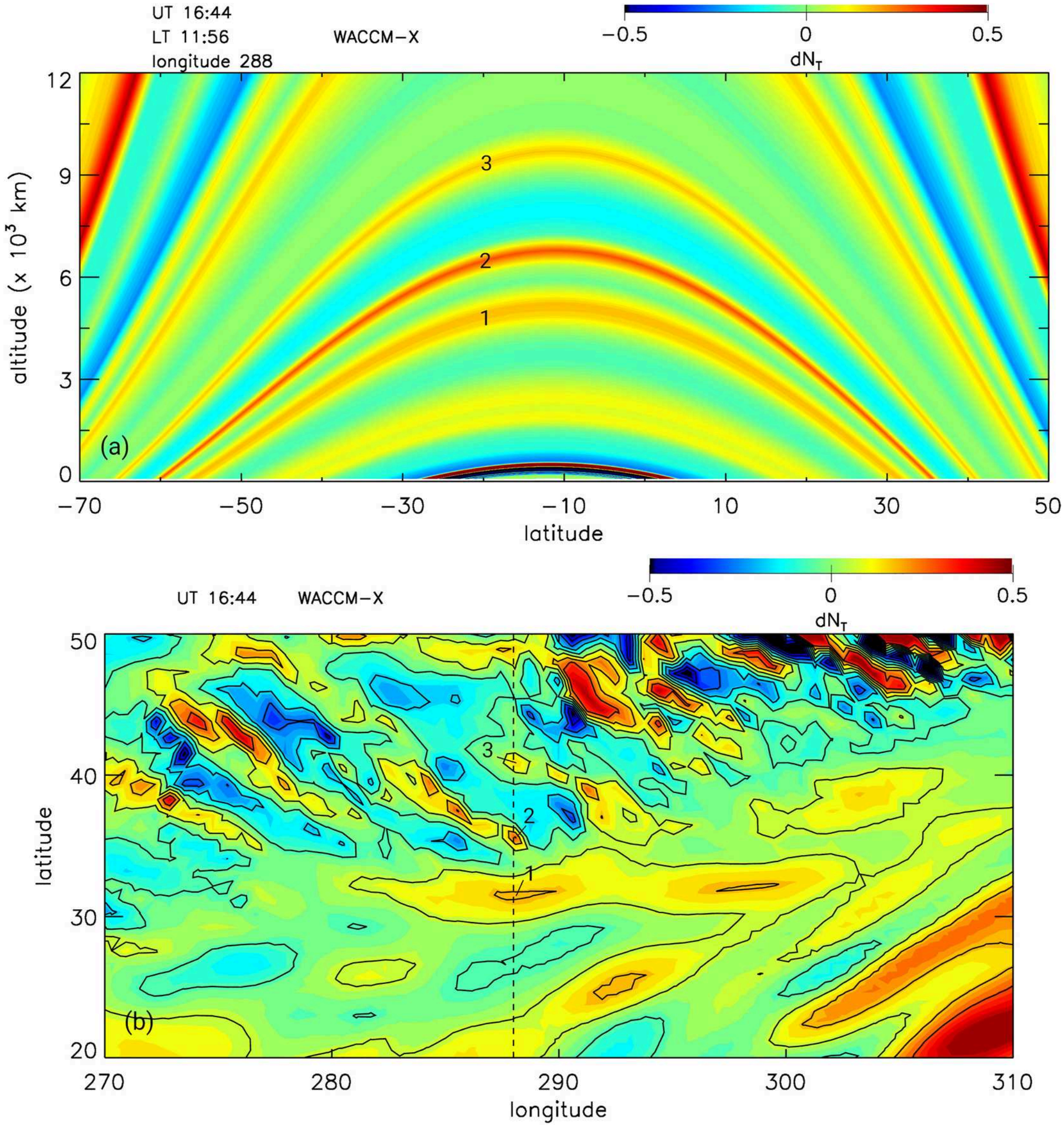

Figure 4. Contour plots of dN_T for WACCM-X at time 16:44 UT as a function of (a) latitude and altitude at longitude 288° (corresponds to 11:56 LT) and (b) longitude and latitude at the base of the field lines.

potential, and in the equatorial region the Appleton ionization crests. In Figure 3b there is very little structure in dN_T. The dotted line at 288° corresponds to the longitude of the contour plot in Figure 3a, and the dark lines are isocontours.

In Figure 4 we show contour plots of dN_T for the WACCM-X case at time 16:44 UT as a function of (a) latitude and altitude at longitude 288° and (b) longitude and latitude at the base of the field lines in the ionosphere. We point out that the local time is 11:56 LT in Figure 4a, that is, it is in the daytime. In sharp contrast to Figure 3a, in Figure 4a are a number of "ducts" at mid-latitudes. Again, the ducts at high-latitudes are associated with variations in the high-latitude convection potential, and in the equatorial region the Appleton ionization crests. Additionally, in Figure 4b there is also considerable small-scale structure in dN_T. The irregularities dN_T are attributed to atmospheric waves in WACCM-X absent in NRLMSISE0/HWM14 that perturb the neutral wind patterns as noted in Equation 1.

In Figures 4a and 4b we also label three ducts: 1, 2, 3. In Figure 4a duct 1 extends to ~32° with a maximum altitude ~4,500 km, duct 2 extends to ~35° with a maximum altitude ~7,000 km, and duct 3 extends to ~40° with a maximum altitude ~9,500 km. These ducts are confined to widths of a few hundred kms in altitude. In Figure 4b we indicate where these ducts map to the ionosphere in longitude and latitude. In these cases, the ducts are also confined to a limited range in both longitude and latitude as noted by the closed isocontours centered about 288°. Thus, these regions of dN_T are consistent with being ducts in that they are confined in altitude, latitude, and longitude.

In Figure 5 we show contour plots of dN_T for the WACCM-X case as a function of latitude and altitude at longitude 288° at times (a) 16:29 UT, (b) 16:44 UT, and (c) 16:59 UT, and have labeled each panel with the positions of ducts 1,2,3 shown in Figure 4a. Over this 30 min period we note that ducts 2 and 3 are maintained albeit at different magnitudes, but duct 1 is not evident at 16:29 UT but only at 16:44 UT and 16:59 UT. Although not shown, ducts 1, 2, and 3 do not occur at earlier or later times (e.g., 16:14 UT and 17:14 UT) at this longitude. Thus, the maximum lifetime of a duct for this case is ∼30 min.

4. Discussion

Clilverd et al. (2007) used data from the CRRES satellite to determine the electron density in the plasmasphere in the range $L = 2.5–5.0$ during solar maximum conditions. Although the focus of the study was on the longitudinal and seasonal variations of the plasmaspheric equatorial electron density, they presented the electron density as a function of longitude and L shell in their Figure 2. We note that the variation they report at $L = 4.0$ is very similar to that shown in Figure 2b. This is not a direct comparison of data and simulation results per se but does indicate that longitudinal variations in the plasmasphere electron density have been observed consistent with model results.

Clilverd et al. (2008) investigated the propagation of ducted and non-ducted whistler wave propagation in range $1.1 < L < 3.0$ using VLF transmitters and plasma wave instruments on the CRRES and DEMETER satellites. They found that for transmitters at $L < 1.5$ most of the whistler wave energy that propagates into the plasmasphere is non-ducted. On the other, whistler wave propagation is predominantly ducted for transmitters at higher L shells (>1.5). For example, in their Figure 5 they show the strongest intensity of whistler waves in the latitude ranges 70°S −40°S and 30°N–50°N in the longitude range 270°–330°. This is consistent with the mid-latitude ducts shown in Figure 4.

Singh et al. (1998) provided a review of plasmaspheric parameters (e.g., equatorial electron density, total electron content along a flux tube, characteristic duct properties) based on whistler spectrograms. In their Table 3 they report prior results related to plasmaspheric ducts. One interesting finding is that the lifetime of ducts is typically in the range 1–2 hr which is also consistent with several of the ducts shown in Figure 4b.

5. Summary

We show that atmospheric gravity waves can generate plasma ducts and irregularities in the plasmasphere using the coupled SAMI3/WACCM-X model. Physically, gravity waves perturb the zonal and meridional neutral winds which affect the plasma motion and electric field. Since the magnetic field lines are equipotentials, the perturbed electric field maps into the plasmasphere and can generate ducts and irregularities. We find the equatorial electron density is irregular as a function of longitude which is consistent with CRRES measurements (Clilverd et al., 2007). We also find that plasma ducts can be generated for L-shells in the range 1.5–3.0 with lifetimes of ∼0.5 hr; we note observations of ducted VLF wave propagation in this L shell range suggest ducted wave lifetimes of 0.5–2 hr (Clilverd et al., 2008; Singh et al., 1998). And lastly, we show that these ducts can form in the daytime in contrast to ducts formed by plasma instabilities which only occur in the nighttime (Helmboldt, 2020b).

One limitation of the current simulation is the grid resolution. The grid spacing at mid-latitudes is ∼70 km so wave-like behavior has scale-sizes $\gtrsim$ 280 km. There have been studies suggesting traveling ionospheric disturbances have wavelengths that peak in the range 50–150 km (Afraimovich et al., 2001). Additionally, studies of whistler wave propagation in the plasmasphere ducts indicate duct widths as small as 10s km (Streltsov & Goyal, 2021). Furthermore, the resolution also limits the number of ducts formed at mid-latitude; in this study we find ∼3–6 ducts can form when there are observations that 15–30 ducts can form (Lester & Smith, 1980) Future work will be to perform higher resolution simulations (e.g., Huba & Joyce, 2010) as well as to determine the dependence of mid-latitude plasma ducts on longitude, season and solar activity, and direct comparisons with observations.

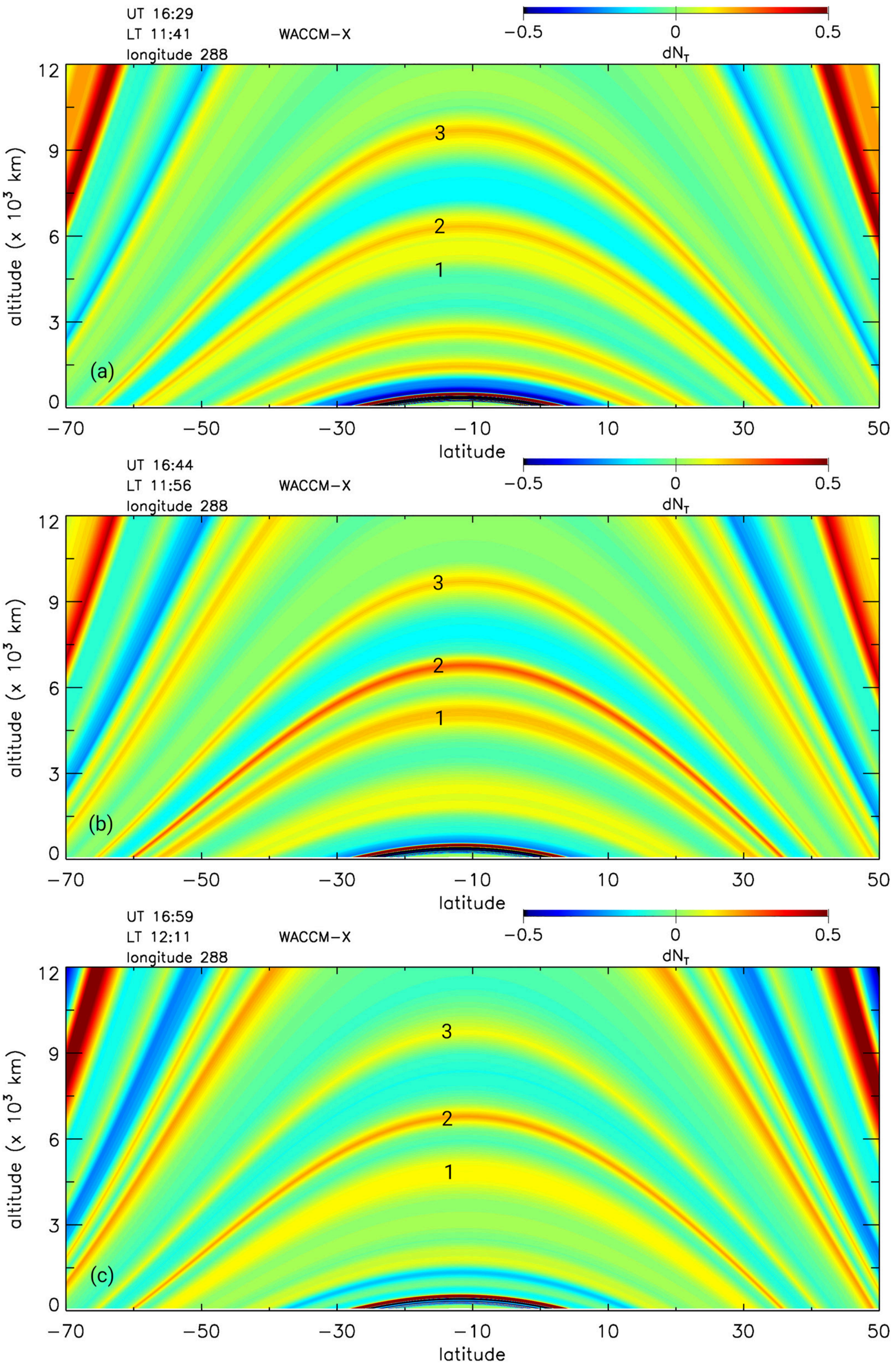

Figure 5. Contour plots of dN_T as a function of latitude and altitude at longitude 288° at times (a) 16:29 UT, (b) 16:44 UT and (c) 16:59 UT.

Data Availability Statement

WACCM-X model (NCAR CESM/WACCM, 2023) and SAMI3 model (Huba, 2023). The data is available at (Huba & Liu, 2023).

Acknowledgments

We thank J.F. Helmboldt and A. Streltsov for critical comments and suggestions to improve the manuscript (JDH). This research was supported by AFOSR (JDH: FA9550-22-C-0001; HLL: FA9550-16-1-0050), NASA (JDH: 80NSSC21K1305; NNG12FA45C/NNG12FA42I; DRIVE Science Center for Geospace Storms (CGS) under award 80NSSC22M0163; HLL: 80NSSC17K0007), and NSF (JDH: AGS-1931415).

References

Afraimovich, E. L., Kosogorov, E. A., Lesyuta, O. S., Ushakov, I. I., & Yakovets, A. F. (2001). Geomagnetic control of the spectrum of traveling ionospheric disturbances based on data from a global GPS network. *Annals of Geophysics*, *19*(7), 723–731. https://doi.org/10.5194/angeo-19-723-2001

Bernhardt, P. A., & Park, C. G. (1977). Protonospheric-ionospheric modeling of VLF ducts. *Journal of Geophysical Research*, *82*(32), 5222–5230. https://doi.org/10.1029/JA082i032p05222

Carpenter, D. L. (1963). Whistler evidence of a 'knee' in the magnetosphere ionization density profile. *Journal of Geophysical Research*, *68*, 1075.

Carpenter, D. L. (1966). Whistler studies of the plasmapause in the magnetosphere 1. Temporal variations in the position of the knee and some evidence on plasma motions near the knee. *Journal of Geophysical Research*, *71*(3), 693–709. https://doi.org/10.1029/jz071i003p00693

Clilverd, M. A., Meredith, N. P., Horne, R. B., Glauert, S. A., Anderson, R. R., Thomson, N. R., et al. (2007). Longitudinal and seasonal variations in plasmaspheric electron density: Implications for electron precipitation. *Journal of Geophysical Research*, *112*(A11), A11210. https://doi.org/10.1029/2007JA012416

Clilverd, M. A., Rodger, C. J., Gamble, R., Meredith, N. P., Parrot, M., Berthelier, J.-J., & Thomson, N. R. (2008). Ground-based transmitter signals observed from space: Ducted or nonducted? *Journal of Geophysical Research*, *113*(A4), A04211. https://doi.org/10.1029/2007JA012602

Cole, K. D. (1971). Formation of field-aligned irregularities in the magnetosphere. *Journal of Atmospheric and Terrestrial Physics*, *33*(5), 741–750. https://doi.org/10.1016/0021-9169(71)90027-4

Cosgrove, R. B., & Tsunoda, R. T. (2002). A direction-dependent instability of sporadic-*E* layers in the nighttime midlatitude ionosphere. *Geophysical Research Letters*, *29*(18), 11-1–11-4. https://doi.org/10.1029/2002GL014669

Darrouzet, F., Gallagher, D. L., André, N., Carpenter, D. L., Dandouras, I., Décréau, P. M. E., et al. (2009). Plasmaspheric density structures and dynamics: Properties observed by the CLUSTER adn IMAGE missions. *Space Science Reviews*, *145*(55), 55–106. https://doi.org/10.1007/s11214-008-9438-9

Drob, D. P., Emmert, J. T., Crowley, G., Picone, J. M., Shepherd, G. G., Skinner, W., et al. (2008). An empirical model of the Earth's horizontal wind fields: HWM07. *Journal of Geophysical Research*, *113*(A12), A12304. https://doi.org/10.1029/2008JA013668

Goldstein, J. (2006). Plasmasphere response: Tutorial and review of recent imaging results. *Space Science Reviews*, *124*(1–4), 203–216. https://doi.org/10.1007/s11214-006-9105-y

Goldstein, J., Spasojević, M., Reiff, P. H., Sandel, B. R., Forrester, W. T., Gallagher, D. L., & Reinisch, B. W. (2003). Identifying the plasmapause in IMAGE EUV data using IMAGE RPI *in situ* steep density gradients. *Journal of Geophysical Research*, *108*(A4), 1147. https://doi.org/10.1029/2002JA009475

Helmboldt, J. F. (2020a). The properties and origins of corotating plasmaspheric irregularities: Part II—Tomography with compact arrays of GPS receivers. *Journal of Geophysical Research: Space Physics*, *125*(6), e2020JA027858. https://doi.org/10.1029/2020JA027858

Helmboldt, J. F. (2020b). Observations of the electrodynamical ties between sporadic *E* and the plasmasphere. *Earth and Space Science*, *7*(11), e2020EA001369. https://doi.org/10.1029/2020EA001369

Helmboldt, J. F., Haiducek, J. D., & Clarke, T. E. (2020). The properties and origins of corotating plasmaspheric irregularities as revealed through a new tomographic technique. *Journal of Geophysical Research: Space Physics*, *125*(3), e2019JA027483. https://doi.org/10.1029/2019JA027483

Huba, J. D. (2023). SAMI3 (version 3.22) [Software]. Zenodo. https://doi.org/10.5281/zenodo.7895859

Huba, J. D., Drob, D. P., Wu, T.-W., & Makela, J. J. (2015). Modeling the ionospheric impact of tsunami-driven gravity waves with SAMI3: Conjugate effects. *Geophysical Research Letters*, *42*(14), 5719–5726. https://doi.org/10.1002/2015GL064871

Huba, J. D., & Joyce, G. (2010). Global modeling of equatorial plasma bubbles. *Geophysical Research Letters*, *37*(17), L17104. https://doi.org/10.1029/2010GL044281

Huba, J. D., Joyce, G., & Fedder, J. A. (2000). SAMI2 (SAMI2 is another model of the ionosphere): A new low-latitude ionosphere model. *Journal of Geophysical Research*, *105*(A10), 23035–23053. https://doi.org/10.1029/2000ja000035

Huba, J. D., & Krall, J. (2013). Modeling the plasmasphere with SAMI3. *Geophysical Research Letters*, *40*(1), 6–10. https://doi.org/10.1029/2012GL054300

Huba, J. D., & Liu, H.-L. (2020). Global modeling of equatorial spread *F* with SAMI3/WACCM-X. *Geophysical Research Letters*, *47*(14), e2020GL088258. https://doi.org/10.1029/2020GL088258

Huba, J. D., & Liu, H.-L. (2023). Modeling plasmasphere irregularities and ducts with SAMI3/WACCM-X [Dataset]. Zenodo. https://doi.org/10.5281/zenodo.8138923

Hurrell, J. W., Holland, M. M., Gent, P. R., Ghan, S., Kay, J. E., Kushner, P. J., et al. (2013). The community Earth system model: A framework for collaborative research. *Bulletin of the American Meteorological Society*, *94*(9), 1339–1360. https://doi.org/10.1175/BAMS-D-12-00121.1

Jacobson, A. R., Hoogeveen, G., Carlos, R. C., Wu, G., Fejer, B. G., & Kelley, M. C. (1996). Observations of inner plasmasphere irregularities with a satellite-beacon radio-interferometer array. *Journal of Geophysical Research*, *101*(A9), 19665–19682. https://doi.org/10.1029/96ja01253

Lemaire, J., Gringauz, K., Carpenter, D., & Bassolo, V. (1998). *The Earth's Plasmasphere (Cambridge atmospheric and space science series)*. Cambridge University Press. https://doi.org/10.1017/CBO9780511600098

Lester, M., & Smith, A. J. (1980). Whistler duct structure and formation. *Planetary and Space Science*, *28*(6), 645–654. https://doi.org/10.1016/0032-0633(80)90011-2

Liu, H.-L., Bardeen, C. G., Foster, B. T., Lauritzen, P., Liu, J., Lu, G., et al. (2018). Development and validation of the whole atmosphere community climate model with thermosphere and ionosphere extension (WACCM-X 2.0). *Journal of Advances in Modeling Earth Systems*, *10*(2), 381–402. https://doi.org/10.1002/2017MS001233

Liu, H.-L., Foster, B. T., Hagan, M. E., McInerney, J. M., Maute, A., Qian, L., et al. (2010). Thermosphere extension of the whole atmosphere community climate model. *Journal of Geophysical Research*, *115*(A12), A12302. https://doi.org/10.1029/2010JA015586

Loi, S. T., Murphy, T., Cairns, I. H., Menk, F. W., Waters, C. L., Erickson, P. J., et al. (2015). Real-time imaging of density ducts between the plasmasphere and ionosphere. *Geophysical Research Letters*, *42*(10), 3707–3714. https://doi.org/10.1002/2015GL063699

NCAR CESM/WACCM. (2023). Community Earth system model 2 (CESM2) (version CESM 2.1.3) [Software]. CESM2. https://doi.org/10.5065/D67H1H0V

Ozhogin, P., Tu, J., Song, P., & Reinisch, B. W. (2012). Field-aligned distribution of the plasmaspheric electron density: An empirical model derived from the IMAGE RPI measurements. *Journal of Geophysical Research*, *117*(A6), A06225. https://doi.org/10.1029/2011JA017330

Perkins, F. (1973). Spread F and ionospheric currents. *Journal of Geophysical Research*, *78*(1), 218–226. https://doi.org/10.1029/JA078i001p00218

Picone, J. M., Hedin, A. E., Drob, D. P., & Aikin, A. C. (2002). NRLMSISE-00 empirical model of the atmosphere: Statistical comparisons and scientific issues. *Journal of Geophysical Research*, *107*(A12), SIA15-1–SIA15-16. https://doi.org/10.1029/2002JA009430

Sandel, B. R., Goldstein, J., Gallagher, D. L., & Spasojevic, M. (2003). Extreme ultraviolet imager observations of the structure and dynamics of the plasmasphere. *Space Science Reviews*, *109*(25), 25–46. https://doi.org/10.1023/b:spac.0000007511.47727.5b

Sandel, B. R., King, R. A., Forrester, W. T., Gallagher, D. L., Broadfoot, A. L., & Curtis, C. C. (2001). Initial results from the IMAGE extreme ultraviolet imager. *Geophysical Research Letters*, *28*(8), 1439–1442. https://doi.org/10.1029/2001gl012885

Singh, R. P., Singh, A. K., & Singh, D. K. (1998). Plasmaspheric parameters as determined from whistler spectrograms: A review. *Journal of Atmospheric and Solar-Terrestrial Physics*, *60*(5), 495–508. https://doi.org/10.1016/s1364-6826(98)00001-7

Sonwalkar, V. S. (2006). The influence of plasma density irregularities on whistler-mode wave propagation. *Geospace Electromagnetic Waves and Radiation*, *6*, 141. https://doi.org/10.1007/3-540-33203-0

Strangeways, H. J. (1982). The effect of multi-duct structure on whistler-mode wave propagation. *Journal of Atmospheric and Terrestrial Physics*, *44*(10), 901–912. https://doi.org/10.1016/0021-9169(82)90043-5

Streltsov, A. V., & Goyal, R. (2021). Whistlers in micro ducts. *Journal of Geophysical Research: Space Physics*, *126*(11), e2021JA029868. https://doi.org/10.1029/2021JA029868

Vadas, S. L., Figueiredo, C., Becker, E., Huba, J. D., Themens, D. R., Hindley, N. P., et al. (2023). Traveling ionospheric disturbances induced by the secondary gravity waves from the Tonga eruption on 15 January 2022: Modeling with MESORAC-HIAMCM-SAMI3 and comparison with GPS/TEC and ionosonde data. *Journal of Geophysical Research: Space Physics*, *128*(6), e2023JA031408. https://doi.org/10.1029/2023JA031408

Weimer, D. R. (2005). Predicting surface geomagnetic variations using ionospheric electrodynamic models. *Journal of Geophysical Research*, *110*(A12), A12307. https://doi.org/10.1029/2005JA011270

Yokoyama, T., Hysell, D. L., Otsuka, Y., & Yamamoto, M. (2009). Three-dimensional simulation of the coupled Perkins and E_s-layer instabilities in the nighttime midlatitude ionosphere. *Journal of Geophysical Research*, *114*(A3), A03308. https://doi.org/10.1029/2008JA013789